


Scaled effective on-site Coulomb interaction in the DFT+ U method for correlated materialsKenji Nawa,^{*} Toru Akiyama, Tomonori Ito, and Kohji Nakamura[†]
*Department of Physics Engineering, Mie University, Tsu, Mie 514-8507, Japan*Tamio Oguchi
*Institute of Scientific and Industrial Research, Osaka University, Ibaraki, Osaka 567-0047, Japan*M. Weinert
Department of Physics, University of Wisconsin-Milwaukee, Milwaukee, Wisconsin 53201, USA (Received 19 June 2017; revised manuscript received 25 December 2017; published 10 January 2018)

The first-principles calculation of correlated materials within density functional theory remains challenging, but the inclusion of a Hubbard-type effective on-site Coulomb term (U_{eff}) often provides a computationally tractable and physically reasonable approach. However, the reported values of U_{eff} vary widely, even for the same ionic state and the same material. Since the final physical results can depend critically on the choice of parameter and the computational details, there is a need to have a consistent procedure to choose an appropriate one. We revisit this issue from constraint density functional theory, using the full-potential linearized augmented plane wave method. The calculated U_{eff} parameters for the prototypical transition-metal monoxides—MnO, FeO, CoO, and NiO—are found to depend significantly on the muffin-tin radius R_{MT} , with variations of more than 2–3 eV as R_{MT} changes from 2.0 to 2.7 a_B . Despite this large variation in U_{eff} , the calculated valence bands differ only slightly. Moreover, we find an approximately linear relationship between $U_{\text{eff}}(R_{\text{MT}})$ and the number of occupied localized electrons within the sphere, and give a simple scaling argument for U_{eff} ; these results provide a rationalization for the large variation in reported values. Although our results imply that U_{eff} values are not directly transferable among different calculation methods (or even the same one with different input parameters such as R_{MT}), use of this scaling relationship should help simplify the choice of U_{eff} .

DOI: [10.1103/PhysRevB.97.035117](https://doi.org/10.1103/PhysRevB.97.035117)

I. INTRODUCTION

In the investigation of the electronic structures of correlated materials such as transition-metal oxides, rare-earth metals, and organometallic molecules, first-principles calculations based on density functional theory (DFT) play a central role, but dealing with correlation effects remains challenging. Efforts to go beyond the (semi-)local density approximation (LDA) to the exchange-correlation functional have attempted to include many-body effects in the DFT framework, e.g., hybrid functional methods with Hartree-Fock, or dynamical mean field theory. On a practical level, the LDA+ U method that introduces Hubbard-model parameters to represent screened on-site Coulomb (U) and exchange (J) interactions is one of the powerful (and conventional) tools suitable for calculations of large systems without expensive computational costs [1–6], and has been used to successfully calculate electronic, magnetic, and optical properties consistent with experiments.

For example, Yang *et al.* [7] demonstrated that in bulk fcc Ni Coulomb correlations treated within the + U method ($U = 1.9$ eV, $J = 1.2$ eV) push degenerate d states away

from the Fermi level, and that this behavior stabilizes the magnetic anisotropy along the [111] direction, in agreement with experiments [8,9], but contrary to $U = 0$ calculations. The + U method was also successfully applied [10] to explain the experimentally observed magnetic switching phenomenon at the BaTiO₃-Fe interface: The trend of the polarization versus the U parameters was used to clarify the magnetoelectricity mechanism at the interface. The + U approach has been essential in areas other than magnetism, including studies of the band gap and phase stability in polymorphic TiO₂ [11], the structural and optical properties of diluted magnetic semiconductors [12], and the ground state electronic configuration in organometallic molecules [13].

The values of U and J are commonly chosen to match experimental observations such as band gaps or oxidation energies. Optimal values of the parameters U and J , however, depend on which exchange-correlation functional is used [14] and the calculated material properties are very sensitive to the values of the on-site Coulomb and exchange terms even in the ground state. More recently the parameters have been calculated directly from first-principles calculations, but these vary over a wide range of values even for the same ionic state in a given material. Table I summarizes some of the previous theoretically calculated effective on-site Coulomb parameters $U_{\text{eff}} = U - J$, for 3d transition-metal monoxides (TMOs). For Mn in MnO, Anisimov and co-workers [15] obtained $U_{\text{eff}} = 6.04$ eV within a constrained LDA approach using

^{*}Current affiliation: Research Center for Magnetic and Spintronic Materials, National Institute for Materials Science (NIMS), Tsukuba, Ibaraki 305-0047, Japan; nawa.kenji@nims.go.jp

[†]kohji@phen.mie-u.ac.jp

TABLE I. Previous calculations of the effective on-site Coulomb interaction $U_{\text{eff}} = U - J$ in eV, for the TM atom (TM = Mn, Fe, Co, Ni) of the monoxide. The first and second columns give the basis sets and method used, respectively.

Basis set ^a	Method ^b	MnO	FeO	CoO	NiO	Ref.
LMTO	cLDA	6.04	5.91	6.88	7.05	[15]
LCAO	cLDA	3.6	4.6	5.0	5.1	[16]
LAPW	cLDA	3.9	3.9	4.2	4.3	[22]
LMTO	cRPA				5.7	[17]
MLWF-PW	cRPA	5.6	4.8	6.3	5.6	[18]
MLWF-LAPW	cRPA	4.9	5.0	5.3	5.9	[19] ^c
MLWF-LAPW	cRPA	5.4	5.5	6.0	6.7	[19] ^d
PW	LR	5.25	4.3	6.1	5.77	[20,21]
PW	LR	4.94	4.10	4.89		[23] ^e
PW	LR	5.52	5.80	5.86		[23] ^f
UHF-MO	ERI		3.7			[24]
PAO	ERI	4.7			7.6	[25]

^aLMTO: Linearized muffin-tin orbitals; LCAO: linear combination of atomic orbitals; LAPW: linearized augmented plane wave; PW: plane wave projected onto localized functions; MLWF: maximally localized Wannier functions; UHF-MO: unrestricted Hartree-Fock molecular orbitals; PAO: pseudoatomic orbitals.

^bcLDA: Constrained LDA; cRPA: constrained random phase approximation; LR: linear response; ERI: determined from electron repulsion integrals.

^c*d* MLWFs.

^d*d* and *p* MLWFs model (a).

^eQuantum-Espresso pseudopotentials.

^fGBRV high-throughput pseudopotentials.

an orthonormalized LMTO basis set, whereas Pickett *et al.* [16] obtained a much smaller value of 3.6 eV using a LCAO basis. Similarly, parameters derived using the constrained random phase approximation (cRPA) [17–19] or the linear response approach of Cococcioni and de Gironcoli [20,21] vary widely depending on the choice of underlying basis (or pseudopotential).

Clearly, comparison of the absolute values of U_{eff} is not always meaningful since theoretically determined parameters can differ significantly depending on the computational setup, e.g., basis set and projection operator [26]. For example, the U values calculated [19] using maximally localized Wannier functions (MLWF) can vary on the order of 1 eV depending on the choice of which bands to include in defining the MLWFs; the choice of pseudopotential [23] and the underlying projectors can have similar effects on U . Unfortunately, this implies that choosing “good” parameters for a specific computational method is problematic without doing a full determination of U_{eff} for each calculation. In the present paper, we revisit the issue of the wide variations in calculated values even when nominally using the same approach. As prototypical examples of strongly correlated materials, we consider the TMOs, which show Mott insulating behavior. The all-electron full-potential linearized augmented plane wave (FLAPW) method has been applied to determine the effective on-site Coulomb interaction parameter U_{eff} for the TM ions (Mn, Fe, Co, and Ni) in the framework of linear response theory using the constraint DFT approach [13]. The U_{eff} values are calculated for different sizes

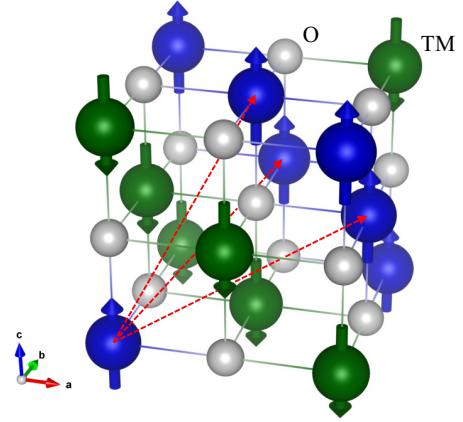


FIG. 1. Atomic structure of transition-metal monoxides with antiferromagnetic alignment along [111] direction. Large (blue and green) circles represent the transition-metals (Mn, Fe, Co, and Ni), including relative spin alignment, while the small (gray) circles represent oxygen atoms. Dashed (red) arrows indicate the lattice vectors of the rhombohedral unit cell.

of muffin-tin (MT) spheres of the TM ions, R_{MT} . We find that the U_{eff} value depends strongly on R_{MT} size in all the systems, varying by more than 2–3 eV. Despite this large variation, the valence band structures obtained for the different optimized U_{eff} values differ only slightly, and we find an approximate scaling of U_{eff} with regard to R_{MT} . Although directly using U_{eff} values in different calculational methods is generally not possible, we propose guidelines for estimating U_{eff} that can provide reasonable values when computational parameters differ.

II. MODEL AND METHOD

A model of the NaCl structure with the type-II antiferromagnetic spin alignment is shown in Fig. 1. The cubic lattice constants are fixed at the experimental values 4.435, 4.334, 4.261, and 4.195 Å for MnO, FeO, CoO, and NiO, respectively [27–30]. All calculations were carried out using the all-electron FLAPW method [31,32] and constraint DFT [33]. The generalized gradient approximation (GGA) is used for exchange-correlation [34] and the $+U$ term in the atomic limit approximation is incorporated in the rotational invariant form [35]. The LAPW basis for the wave functions in the interstitial $e^{i(\mathbf{k}+\mathbf{G})\cdot\mathbf{r}}$ has a cutoff of $|\mathbf{k} + \mathbf{G}| \leq 3.9 a_B^{-1}$, and the angular momentum expansion inside the sphere is truncated at $\ell = 8$ for the transition-metal atom and at 6 for the oxygen. (For the potential and density $|\mathbf{G}| \leq 9.8 a_B^{-1}$.) The scalar-relativistic radial functions $u_\ell(r)$ and their energy derivatives $\dot{u}_\ell(r)$ are obtained for the self-consistent spherical potential $V_{\ell=0}(r)$ at the energy parameters ϵ_ℓ that are adjusted self-consistently throughout the calculations [36]. For the oxygen atom, the MT radius was fixed at $1.4 a_B$, while that of the TM atoms was varied from $2.0 a_B$ up to (almost) touching spheres. The angular momentum expansion of the LAPW wave functions allows for the straightforward calculation of the on-site density matrix for a given ℓ by making use of the projection operator onto the

$\ell mm'$ subspace

$$\hat{P}_{m'm}^\ell = |u_\ell Y_{\ell m'}\rangle \langle u_\ell Y_{\ell m}| + \frac{1}{\langle \dot{u}_\ell | \dot{u}_\ell \rangle} |\dot{u}_\ell Y_{\ell m'}\rangle \langle \dot{u}_\ell Y_{\ell m}|. \quad (1)$$

The d occupation on a site is then given simply as the trace of the local $\ell = 2$ block of the density matrix.

To put the calculations in context, we give a brief review of the linear response approach to the calculation of $+U$ following Ref. [20]. The physical interpretation of $+U$ is that it is the unphysical contributions to the curvature of the total energy $\partial^2 E[\{q_\alpha\}]/\partial q_\alpha^2$, arising from the approximate exchange-correlation functional at nonintegral occupations q_α of localized states. (α is an orbital/site index.) In a solid, however, hybridization effects also lead to quadratic terms that *are* physical and not related to U . These “band structure” (kinetic energy) contributions must be subtracted, and thus the U_{eff} values are given by the difference between the second derivatives of the total energies corresponding to the interacting (screened) system E^{scf} and the noninteracting (traditionally referred to as Kohn-Sham [20]) one E^{KS} that includes only the (re)hybridization effects:

$$U_{\text{eff}}^\alpha = \frac{\partial^2 E^{\text{scf}}[\{q_\alpha\}]}{\partial q_\alpha^2} - \frac{\partial^2 E^{\text{KS}}[\{q_\alpha\}]}{\partial q_\alpha^2}. \quad (2)$$

To obtain the derivatives of the total energies $E^X[\{q_\alpha\}]$ ($X = \text{scf}, \text{KS}$) requires varying (and fixing) q_α and is done using constraint DFT [37]:

$$E^X[\{q_\alpha\}] = \min_{n(\mathbf{r}), \mu_\alpha} \left\{ E_{\text{GGA}}^X[n(\mathbf{r})] + \sum_\alpha \mu_\alpha (n_\alpha - q_\alpha) \right\}, \quad (3)$$

where the Lagrange multipliers μ_α enforce the constraint on the occupations n_α . Since

$$\frac{\partial}{\partial q_\alpha} E^X[\{q_\alpha\}] = -\mu_\alpha, \quad \frac{\partial^2}{\partial q_\alpha^2} E^X[\{q_\alpha\}] = -\frac{\partial \mu_\alpha}{\partial q_\alpha}, \quad (4)$$

μ_α and q_α are conjugate variables, and a Legendre transformation leads to the computationally more tractable case with the constraint fields as the independent variables:

$$E^X[\{\mu_\alpha\}] = \min_{n(\mathbf{r})} \left\{ E_{\text{GGA}}^X[n(\mathbf{r})] + \sum_\alpha \mu_\alpha n_\alpha \right\}. \quad (5)$$

The last term leads to an additional potential contribution in the single-particle Kohn-Sham equations of the form $\sum_\alpha \mu_\alpha P^\alpha$ where P^α is a projection operator for the given orbital. By introducing the nonlocal linear density response functions

$$(\chi_{\text{scf}})_{\beta\alpha} = \frac{\partial n_\beta}{\partial \mu_\alpha}, \quad (\chi_{\text{KS}})_{\beta\alpha} = \frac{\partial n_\beta^{\text{KS}}}{\partial \mu_\alpha}, \quad (6)$$

and noting that for both

$$\frac{\partial \mu_\alpha}{\partial n_\alpha} = (\chi_X^{-1})_{\alpha\alpha} = -\frac{\partial^2}{\partial q_\alpha^2} E^X[\{q_\alpha\}], \quad (7)$$

the effective U_{eff}^α parameter is obtained from

$$U_{\text{eff}}^\alpha = (\chi_{\text{KS}}^{-1} - \chi_{\text{scf}}^{-1})_{\alpha\alpha}. \quad (8)$$

The elements of the matrix χ_{scf} are obtained numerically from self-consistent (fully screened) calculations in the presence of the local perturbation μ_α ; those of χ_{KS} are obtained from

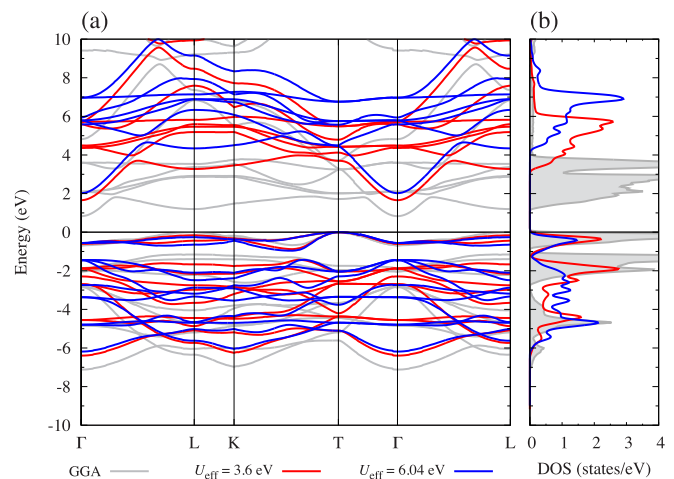


FIG. 2. (a) Band structure and (b) partial $3d$ density of states for MnO, for $R_{\text{MT}}(\text{Mn}) = 2.2 a_B$. Red and blue solid lines correspond to the previously reported values of U_{eff} of 3.6 and 6.04 eV, respectively (see Table I). The GGA calculation ($U_{\text{eff}} = 0$ eV) is also shown as the gray line in (a) and filled area in (b). The energy zero is set to the top of the valence band.

the first iteration of the self-consistent procedure starting from the self-consistent GGA density, i.e., corresponding to the “noninteracting” hybridization changes in occupation due to the local perturbation μ_α . These response matrices are calculated for various size supercells to minimize artifacts arising from periodic boundary conditions [20]. Although this approach can be extended [38] straightforwardly by repeating this procedure until self-consistent values of U_{eff} are obtained, we have limited the calculations to a single cycle and to finding a single U_{eff} for the transition-metal d orbitals.

III. RESULTS AND DISCUSSIONS

We start by considering the effect of U_{eff} on the band structure. Figure 2 shows the calculated bands and partial densities of states (DOS) of the $3d$ bands for MnO for two U_{eff} values previously derived (cf. Table I), 3.6 and 6.04 eV, as well as GGA, $U_{\text{eff}} = 0$, for $R_{\text{MT}} = 2.2 a_B$. In the GGA, there are sharp peaks due to the Mn $3d$ states around the Fermi energy. Introducing U_{eff} opens the gap and pushes the Mn d states away. Not surprisingly, the choice of U_{eff} affects both the valence and conduction bands significantly, and highlights the nontransferability of U_{eff} values.

We now proceed to calculate U_{eff} . Figure 3 shows the occupation numbers of $3d$ orbitals n_d of the TM atoms as a function of applied constraint field μ for R_{MT} varying from 2.0 to 2.7 a_B . In all the systems, the occupation number increases as R_{MT} increases. When a negative (or positive) constraint field is applied, the occupation number at the constrained TM atoms linearly increases (decreases) relative to the $\mu = 0$ case (left panels in Fig. 3). Since the total occupation number in the unit cell is conserved, the occupation numbers at the unconstrained ($\mu = 0$) nearest-neighbor site exhibit the opposite tendency (right panels).

The response functions of Eq. (6), corresponding to the gradient of occupation number n_β with respect to the applied

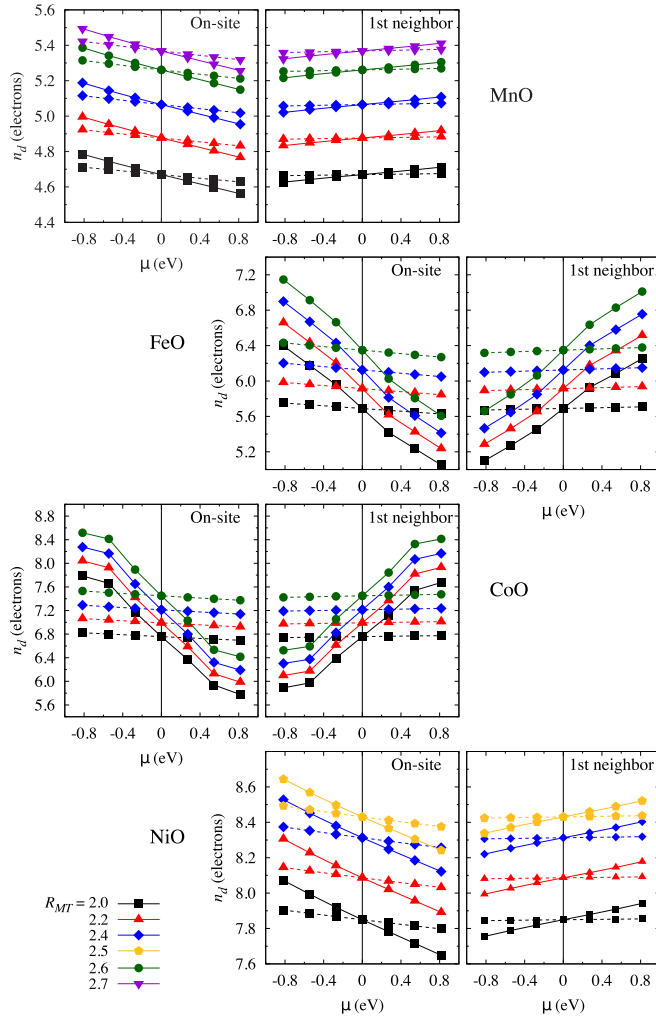


FIG. 3. Variations of the occupation numbers of $3d$ orbitals n_d as a function of constraint field μ for MnO, FeO, CoO, and NiO. Left panels are for the site where μ is applied; right panels are at the unconstrained first-neighbor site. Solid and dashed lines are for the Kohn-Sham (KS) and self-consistent (scf) calculations, respectively. The different symbols (and colors) correspond to different sphere radii (in a_B) of the TM atoms.

constraint field μ_α at site α , were calculated numerically for each site β , and then U_{eff} was evaluated from Eq. (8). Because the KS term does not include self-consistent screening, the change in bands energies—and hence occupation numbers n_d —due to the applied constraint fields, can be understood in terms of perturbation theory: the curves for n_d for different R_{MT} (solid lines in Fig. 3) are parallel to each other, and thus results in approximately constant χ_{KS} . On the other hand, the interacting χ_{scf} is calculated self-consistently, with the screened response obtained by treating the interactions of the electrons, nuclei, and exchange-correlation at GGA level. Since the self-consistency cycle is beyond the framework of linear response, the variation of n_d with regard to μ is consequently affected by the size of the MT sphere differently.

As mentioned above, Eq. (8) requires the inverses of the density response matrices, which in turn depend on the size of the supercells. Figure 4 summarizes the behavior of U_{eff} as a

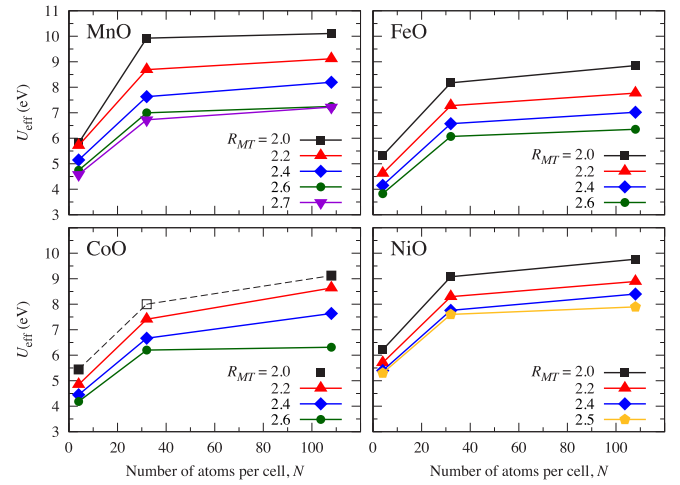


FIG. 4. Calculated effective on-site Coulomb interaction parameters U_{eff} as a function of the number of atoms per cell N for MnO, FeO, CoO, and NiO. For CoO, the open square for $R_{\text{MT}} = 2.0 a_B$ is the expected value based on the trends observed for the other systems (see text for more details). Notation is the same as in Fig. 3.

function of number of atoms per cell (size of the supercell). For MnO with $R_{\text{MT}} = 2.0 a_B$, for example, U_{eff} has a value of 5.8 eV for a $1 \times 1 \times 1$ supercell (4 atoms per cell), while for $2 \times 2 \times 2$ (32 atoms) and $3 \times 3 \times 3$ supercells (108 atoms) it converges to 10.1 eV. For all the systems the converged U_{eff} values decrease as the sphere radius increases. These changes can be quite large, such as in the case of MnO (Fig. 4) where there is a 3 eV difference in U_{eff} for radii of 2.0 and 2.7 a_B . Similar behavior is seen for FeO and NiO; the results of CoO will be discussed later.

Although the calculated U_{eff} varies significantly with MT radius, the valence band structures and local $3d$ -DOS vary only weakly as shown in Fig. 5, but are qualitatively (and physically) different from the GGA results. That consistently derived values of $U_{\text{eff}}(R_{\text{MT}})$ do in fact result in the same band structures and properties argues strongly for the validity of the underlying constraint DFT approach and demonstrates that different (converged) DFT computational methods should agree even when the absolute values of U_{eff} differ greatly. This “invariance” of the valence band structure (Fig. 5) when using optimized U_{eff} values is in contrast (cf. Fig. 2) to the qualitative and quantitative changes that occur when U is varied by a similar amount keeping other computational parameters the same.

Based on our results, we propose guidelines to estimate suitably scaled values of U_{eff} for different MT sphere size, which will also be applicable to other computational methods. Figure 6 shows the $U_{\text{eff}}(R_{\text{MT}})$ as a function of occupation number $n_d(R_{\text{MT}})$ determined in the standard $U = 0$ GGA calculations. We find a simple linear relationship between U_{eff} and n_d : U_{eff} is negatively proportional to increasing n_d as shown by the regression lines in the figure. We have confirmed for a number of cases that using U_{eff} values estimated from the calculated d -electron occupation number at the GGA level produces basically the same band structure and gives the same physics.

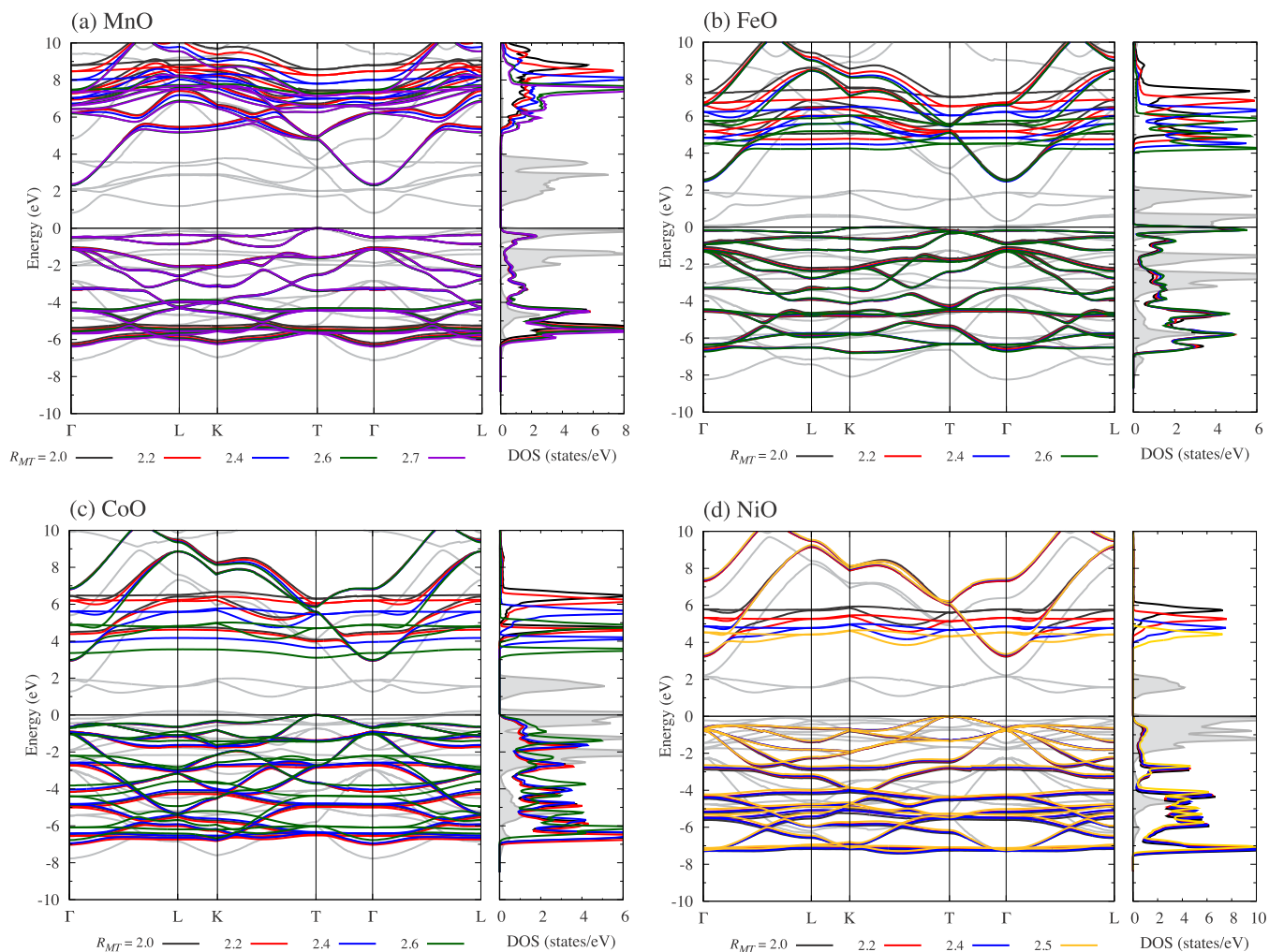


FIG. 5. GGA+ U band structures and partial 3d densities of states for different TM sphere radii using the calculated $U_{\text{eff}}(R_{\text{MT}})$ values. The GGA calculations ($U_{\text{eff}} = 0$ eV) are also shown in gray. The energy zero is set to the top of the valence band.

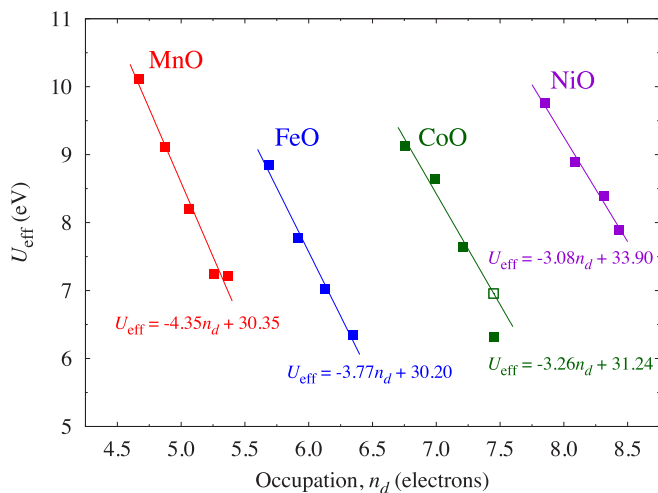


FIG. 6. Calculated U_{eff} values as a function of GGA ($U = 0$) occupation numbers $n_d(R_{\text{MT}})$ for various sphere radii (solid squares) for MnO, FeO, CoO, and NiO. Regression lines are also shown by solid lines. For CoO system, the open square corresponds to the expected scaled value for $R_{\text{MT}} = 2.6 a_B$.

A comparison of the U_{eff} values in Figs. 4 and 6 (and in Table I) shows that MnO does not follow the expected trend of U_{eff} increasing as one moves to the right in the TM series. This result may be even more surprising in that the bare Coulomb integrals do follow the naive expectation. Although we do not have a rigorous explanation, we can make some observations. MnO is qualitatively different from the other TMOs in that the Mn d^5 configuration is fully polarized, and thus it is more difficult to change the d occupation compared to Fe, Co, and Ni where the local minority d orbitals are partially occupied. This aspect is reflected in the significantly smaller slopes (χ_{KS}) in Fig. 3. In addition, the on-site ratios $\chi_{\text{KS}}/\chi_{\text{scf}}$ are also smaller for MnO. Analysis of these on-site contributions suggest that the larger value of U_{eff} for Mn can be attributed to χ_{scf} being smaller than expected if the naive trend for U_{eff} were to hold. We speculate that the origin of this behavior may be related to the standard spin scaling in GGA and LSDA functionals that interpolates between the nonmagnetic and fully polarized limits: The Mn d local states are fully polarized, but the spin fraction ζ entering the exchange-correlation functionals is not because of the unpolarized core and sp electrons (as

well as the oxygen tails). In this scenario, the larger U_{eff} is needed to push the spin fraction towards the fully polarized limit.

Of the different TMOs considered, CoO presented some particular issues which we now discuss. In Fig. 4 we were unable to obtain a value for the $R_{\text{MT}} = 2.0 a_B$ $2 \times 2 \times 2$ (32 atom) supercell because our calculations did not yield a stationary solution for this antiferromagnetic alignment, but we were able to obtain one for the larger $3 \times 3 \times 3$ (108 atom) cell and for different R_{MT} values. However, an approximate value could be obtained from the scaling behavior and is represented by the opened square and dashed line in Fig. 4. Rather unexpectedly, the behavior for $R_{\text{MT}} = 2.6 a_B$ with regard to cell size differs from the others, with a value of $U_{\text{eff}} = 6.3$ eV for the largest cell considered. This value is smaller than expected from other trends, and in fact leads to a calculated band structure [the green line in Fig. 5(c)] that differs from the others, with a noticeable shift of the 3d states. Similarly, in Fig. 6, only the $R_{\text{MT}} = 2.6 a_B$ point is off the regression line for CoO. While further investigations would be needed to definitely determine why this point is off the line, analysis of the calculations suggest that the observed behavior for this $3 \times 3 \times 3$ cell with almost ($\sim 0.026 a_B$) touching Co and O spheres is due to numerical issues related to difficulties in obtaining the self-consistent solution. (As a practical matter, touching spheres in FLAPW calculations are *not* good practice, since ensuring continuity of the wave functions at the touching points is difficult.) These convergence issues caused noise in the calculation of the occupation changes of the far neighbors, affecting the calculated inverse response functions, and leading to an U_{eff} almost the same as for the $2 \times 2 \times 2$ supercell. Having plausible (technical) reasons for the discrepancy (and understanding what would need to be done to obtain a consistent value), we did not redo the calculation since it would not have provided any new insights. Instead, we use this case to illustrate both (i) the possible sensitivity of the calculation of U_{eff} to computational details and (ii) the use of the scaling relationship: The scaled value of 7.0 eV, as indicated by the open square in Fig. 6 appropriate for $R_{\text{MT}} = 2.6 a_B$, gives a valence band structure (not shown) that overlays those for $U_{\text{eff}}(R_{\text{MT}})$, $R_{\text{MT}} = 2.0, 2.2$, and $2.4 a_B$.

Although the valence band structures for different values of $U_{\text{eff}}(R_{\text{MT}})$ vary only slightly, there are larger differences in the conduction bands (Fig. 5). Using MnO as an example, a plausible explanation involves the nature of antibonding wave function. The Mn 3d states just below the Fermi energy hybridize with O 2p orbitals in the GGA calculation [Fig. 7(a)]. In contrast, for GGA+ U , the O 2p predominates at the Fermi level [Fig. 7(b)]. Figure 7(c) shows a schematic energy diagram of the hybridization between Mn and O in the GGA and GGA+ U calculations. For the majority valence (occupied) states, the introduction of the + U correction pushes the Mn 3d orbitals down to lower energy relative to the O 2p, hybridizing to form bonding orbitals, rather than antibonding states in GGA calculation. Both with and without + U , antibonding states are formed by Mn 3d states in the minority conduction (unoccupied) bands. The wave functions of the antibonding state, which possesses a node, are more compact spatially compared to those of bonding states. Thus, the weight of an antibonding states varies slower with respect to sphere size

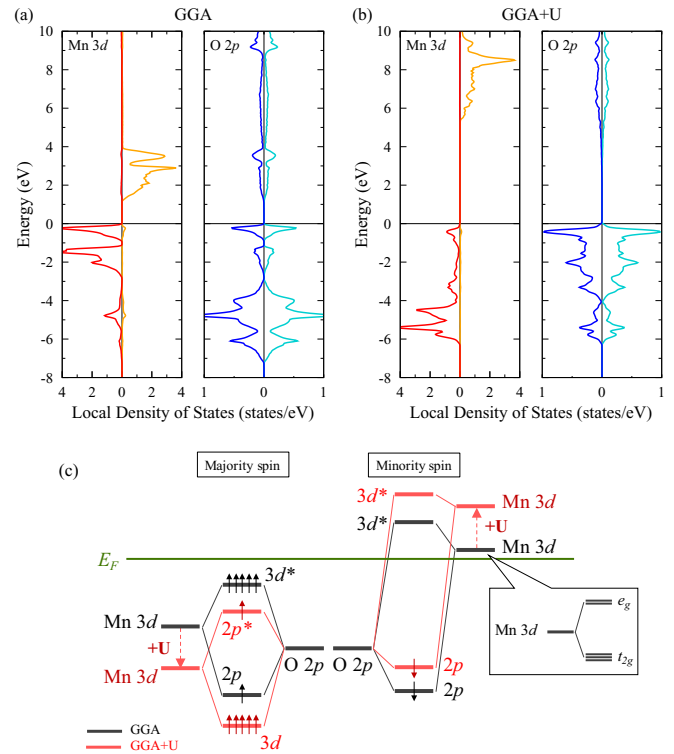


FIG. 7. Calculated spin-resolved local DOS for MnO for (a) GGA ($U_{\text{eff}} = 0$) and (b) GGA+ U for $R_{\text{MT}} = 2.2 a_B$. (Note the different energy ranges for the Mn and O DOS.) (c) Energy diagram showing the hybridization between Mn 3d and O 2p orbitals in GGA (black) and GGA+ U (red) calculations. (The e_g and t_{2g} splitting of the Mn 3d orbitals is ignored for simplicity.)

than the bonding ones; this is one reason behind the decrease in magnitude of the observed slopes in Fig. 6 going from Mn to Ni. A consequence is that for the conduction bands, changing R_{MT} does not appreciably change the d wave function weight that U is acting on, so the size of the matrix elements are mainly determined by the value of U_{eff} alone. As a result, for all the systems considered, the conduction bands are shifted to lower energy as R_{MT} increases, as shown in Fig. 5, as U_{eff} decreases.

IV. SUMMARY

The on-site Coulomb effective parameters U_{eff} for the prototypical correlated TMOs were determined using the all-electron FLAPW method based on constraint DFT approach within a linear response theory. Although a significant dependence of the U_{eff} value on R_{MT} is clearly found, this dependence leads to relatively small variations in physical properties, including the valence band structure, provided the calculations are carried out with U_{eff} values appropriate for the choice of R_{MT} . This behavior can be understood from a scaling argument relating U_{eff} and n_d calculated in the standard GGA. Our results implies that simple transferability of U_{eff} values among different calculation methods is not allowed, but the scaling arguments can be used to guide the choice of suitable + U parameter.

ACKNOWLEDGMENTS

Work at Mie University and Osaka University was supported in part by the Japan Society for the Promotion of Science KAKENHI Grants No. JP16J07422 and No. JP16H02267, and by the Research Program of “Dynamic Alliance for Open Innovation Bridging Human, Environment and Mate-

rials” in “Network Joint Research Center for Materials and Devices,” Grants No. 20175023 and No. 20174022. Work at UWM was supported by the National Science Foundation DMREF-1335215. Computations were performed at the Research Institute for Information Technology, Kyushu University.

-
- [1] V. I. Anisimov, I. V. Solovyev, M. A. Korotin, M. T. Czyżyk, and G. A. Sawatzky, *Phys. Rev. B* **48**, 16929 (1993).
- [2] I. V. Solovyev, P. H. Dederichs, and V. I. Anisimov, *Phys. Rev. B* **50**, 16861 (1994).
- [3] V. I. Anisimov, F. Aryasetiawan, and A. I. Liechtenstein, *J. Phys. Condens. Matter* **9**, 767 (1997).
- [4] P. W. Anderson, *Phys. Rev.* **124**, 41 (1961).
- [5] J. Hubbard, *Proc. R. Soc. London Ser. A* **276**, 238 (1964).
- [6] A. I. Liechtenstein, V. I. Anisimov, and J. Zaanen, *Phys. Rev. B* **52**, R5467(R) (1995).
- [7] I. Yang, S. Y. Savrasov, and G. Kotliar, *Phys. Rev. Lett.* **87**, 216405 (2001).
- [8] C. S. Wang and J. Callaway, *Phys. Rev. B* **9**, 4897 (1973).
- [9] F. Weling and J. Callaway, *Phys. Rev. B* **26**, 710 (1982).
- [10] G. Radaelli, D. Petti, E. Plekhanov, I. Fina, P. Torelli, B. R. Salles, M. Cantoni, C. Rinaldi, D. Gutiérrez, G. Panaccione, M. Varela, S. Picozzi, J. Fontcuberta, and R. Bertacco, *Nat. Commun.* **5**, 3404 (2014).
- [11] M. E. Arroyo-de Dompablo, A. Morales-Garcia, and M. Taravillo, *J. Chem. Phys.* **135**, 054503 (2011).
- [12] A. Abbad, H. A. Bentounes, W. Benstaali, S. Bentata, and B. Bouadjemi, *Chalcogenide Lett.* **12**, 301 (2015).
- [13] K. Nawa, Y. Kitaoka, K. Nakamura, H. Imamura, T. Akiyama, T. Ito, and M. Weinert, *Phys. Rev. B* **94**, 035136 (2016).
- [14] C. Loschen, J. Carrasco, K. M. Neyman, and F. Illas, *Phys. Rev. B* **75**, 035115 (2007).
- [15] V. I. Anisimov, J. Zaanen, and O. K. Andersen, *Phys. Rev. B* **44**, 943 (1991).
- [16] W. E. Pickett, S. C. Erwin, and E. C. Ethridge, *Phys. Rev. B* **58**, 1201 (1998).
- [17] K. Karlsson, F. Aryasetiawan, and O. Jepsen, *Phys. Rev. B* **81**, 245113 (2010).
- [18] B.-C. Shih, T. A. Abtey, X. Yuan, W. Zhang, and P. Zhang, *Phys. Rev. B* **86**, 165124 (2012).
- [19] R. Sakuma and F. Aryasetiawan, *Phys. Rev. B* **87**, 165118 (2013).
- [20] M. Cococcioni and S. de Gironcoli, *Phys. Rev. B* **71**, 035105 (2005).
- [21] A. Floris, S. de Gironcoli, E. K. U. Gross, and M. Cococcioni, *Phys. Rev. B* **84**, 161102(R) (2011).
- [22] H. Jiang, R. I. Gomez-Abal, P. Rinke, and M. Scheffler, *Phys. Rev. B* **82**, 045108 (2010).
- [23] Z. Xu, Y. V. Joshi, S. Raman, and J. R. Kitchin, *J. Chem. Phys.* **142**, 144701 (2015).
- [24] N. J. Mosey, P. Liao, and E. A. Carter, *J. Chem. Phys.* **129**, 014103 (2008).
- [25] L. A. Agapito, S. Curtarolo, and M. Buongiorno Nardelli, *Phys. Rev. X* **5**, 011006 (2015).
- [26] E. R. Ylvisaker, W. E. Pickett, and K. Koepernik, *Phys. Rev. B* **79**, 035103 (2009).
- [27] C. A. McCammon and L. Liu, *Phys. Chem. Miner.* **10**, 106 (1984).
- [28] L. F. Mattheiss, *Phys. Rev. B* **5**, 290 (1972).
- [29] R. Kannan and Mohindar S. Seehra, *Phys. Rev. B* **35**, 6847 (1987).
- [30] S. L. Dudarev, A. I. Liechtenstein, M. R. Castell, G. A. D. Briggs, and A. P. Sutton, *Phys. Rev. B* **56**, 4900 (1997).
- [31] E. Wimmer, H. Krakauer, M. Weinert, and A. J. Freeman, *Phys. Rev. B* **24**, 864 (1981).
- [32] M. Weinert, E. Wimmer, and A. J. Freeman, *Phys. Rev. B* **26**, 4571 (1982).
- [33] K. Nakamura, Y. Kitaoka, T. Akiyama, T. Ito, M. Weinert, and A. J. Freeman, *Phys. Rev. B* **85**, 235129 (2012).
- [34] J. P. Perdew, K. Burke, and M. Ernzerhof, *Phys. Rev. Lett.* **77**, 3865 (1996).
- [35] A. B. Shick, A. I. Liechtenstein, and W. E. Pickett, *Phys. Rev. B* **60**, 10763 (1999).
- [36] M. Weinert, G. Schneider, R. Podloucky, and J. Redinger, *J. Phys. Condens. Matter* **21**, 084201 (2009).
- [37] P. H. Dederichs, S. Blügel, R. Zeller, and H. Akai, *Phys. Rev. Lett.* **53**, 2512 (1984).
- [38] H. J. Kulik, M. Cococcioni, D. A. Scherlis, and N. Marzari, *Phys. Rev. Lett.* **97**, 103001 (2006).